Electrical Engineering Theses and Dissertations

Electrical Engineering

Design of a Drone-Flight-Enabled Wireless Isolation Chamber

John Wensowitch
jwensowitch@smu.edu

DESIGN OF A DRONE-FLIGHT-ENABLED

WIRELESS ISOLATION CHAMBER

Approved by:

DocuSigned by:

Joseph Camp

9511A4DC14DF463...

Dr. Joseph Camp
Associate Professor

DocuSigned by:

Dinesh Rajan

EF0377D1F64E4D2...

Dr. Dinesh Rajan
Professor

DocuSigned by:

Bruce Gnade

7DBA525A52DD44A...

Dr. Bruce Gnade
Clinical Professor

DESIGN OF A DRONE-FLIGHT-ENABLED

WIRELESS ISOLATION CHAMBER

A Thesis Presented to the Graduate Faculty of the

Bobby B. Lyle School of Engineering

Southern Methodist University

in

Partial Fulfillment of the Requirements

for the degree of

Master of Science

in

Electrical Engineering

by

John Wensowitch

B.S., Electrical Engineering, Southern Methodist University

May 16, 2020

Wensowitch, John   B.S., Electrical Engineering, Southern Methodist University

Design of a Drone-Flight-Enabled
Wireless Isolation Chamber

Advisor: Dr. Joseph Camp

Master of Science degree conferred May 16, 2020

Thesis completed April 29, 2020

Drone-based applications are already seeing tremendous adoption across a variety of industries, including photography and inspection services, while next-generation applications such as last-mile delivery, wireless services, and even transportation are beginning to emerge. To this end, efforts have worked to manage and coordinate multiple drones, and drones have already been used in wireless research to measure the unique wireless characteristics in various environments associated with drone-based communications. In particular, the propagation of the wireless signal from the perspective of the drone is of increased interest due to the unique mobility and freedom in all three-dimensions that drones offer in contrast to traditional ground-based wireless communications. In parallel, wireless testbeds have been created that seek to isolate and evaluate emerging concepts such as highly-directional and distributed wireless communications, often associated with the fifth-generation (5G) of wireless communications technologies. These advances rely on coordination among an increasing number of wireless nodes with substantially more antennas to provide a greater degree of wireless channels and improved signal quality for increased data throughput. However, the intersection of these families of works does not directly focus on characterizing the impact that a drone has on wireless communications. The unique drone-based aspects that have been separately identified include: (*i.*) the drone's structure and size, (*ii.*) the type of antenna, as well as its placement and orientation on the drone, and (*iii.*) the dis-

tributed and dynamic coordination among multiple drones, better known as drone swarms. To better understand and study the culmination of these aspects in the three-dimensional space that drones operate requires a controlled, repeatable in-flight environment with a surrounding wireless testbed infrastructure. In this work, we design a drone-flight-enabled isolation chamber to capture complex spatial wireless channel relationships that drone links experience as applications scale from single-drone to swarm-level networks within a shared three-dimensional space. Driven by the challenges of outdoor experimentation, we identify the need for a highly-controlled indoor environment where external factors can be mitigated. To do so, we first build an open-source drone platform to provide programmable control with visibility into the internal flight control system and sensors enabling specialized coordination and accurate repeatable positioning within the isolated environment. We then design a wireless data acquisition system and integrate distributed software-defined radios (SDRs) to inspect multi-dimensional wireless behavior from the surrounding area. We achieve and demonstrate the value of measurement perspectives from diverse altitudes and spatial locations with the same notion of time. Finally, we demonstrate how multi-dimensional models from experimental measurements can be implemented to simulate multi-drone networks on a practical scale.

TABLE OF CONTENTS

LIST OF FIGURES

ix

LIST OF TABLES

Introduction

1.1. Motivation

The unique perspective that drones provide makes them an attractive tool for numerous commercial applications. With over 436k commercial drones registered with the Federal Aviation Administration (FAA) as of February 2020 [1] and with the current projection for the number of commercial registrations to be 2 to 3 years early [2], many industries are quickly adopting drones for their operations. As drones move from single-platform, on-demand use cases to those with cooperative networks of nodes, it is important to understand the spatially-distributed challenges these wireless links face. Furthermore, due to the dynamic nature of drone nodes joining and leaving a localized wireless network (ad hoc) and the intricacy of next-generation, multi-antenna wireless protocols, it is imperative to fully characterize these complex wireless channels across spatial distributions in the horizontal and vertical dimensions.

There are several works utilizing drones for a variety of purposes, such as measuring cellular coverage and interference [3–5], servicing Internet of Things (IoT) devices [6], and testbeds for developing enhanced vehicular control algorithms [7–9]. Some works characterize the multi-dimensional propagation environment from a drone's perspective as well as the impact of antenna orientation in outdoor environments [10, 11]. There also exist wireless testbeds investigating next-generation wireless technologies and distributed networks for a variety of applications [12–16] as well as unique methods for distributed clocking [17]. However, these works do not provide the necessary infrastructure to fully join these efforts

and characterize the complex multi-dimensional aspects that drone-based communications present.

1.2. Background

Our background in outdoor experimental measurement studies provided us with a perspective on how to approach the design of the drone-flight-enabled wireless isolation chamber. In our studies, we have explored the complex behaviors of wireless signals traveling through space in various environments from the perspective of users [18], mobile vehicles [19], and various drone-based scenarios [20–23]. In our studies concerning drones, we have examined how drone communications are affected by the transmission and reception of wireless signals to nodes on the ground, as well as to another drone in the air.

When assessing how wireless signals are affected by communicating on a drone, we identified several concepts that have shaped our measurements and understanding. One of the major effects that any wireless communication faces are how the signal is modified or attenuated, as it travels through space, a concept commonly known as path loss. A standard antenna is typically estimated as a point source that radiates equal power in all directions or omnidirectionally. When this power radiates in all directions through the air with no physical obstructions in its path, it is considered free-space path loss. However, even air causes this power density to quickly degrade exponentially following an inverse-square law. When a drone is communicating at a high enough altitude with another drone, we consider this a perfect line-of-sight, free space environment and this tends to be the best-case scenario for the attenuation of wireless signals.

However, once a drone begins communicating to a node on or near the ground several other factors are introduced and it can no longer be considered free-space propagation. The ground itself and any other obstacles around the ground can cause the wireless signal to

be reflected, absorbed, diffracted, scattered, and refracted by various objects and materials. These various electromagnetic wave behaviors can drastically alter the wireless path that a signal travels. As these paths are comprised of various distances and experience different levels of attenuation, this creates multiple communication paths in both space and time from the perspective of a drone. Figure 1.1 illustrates how two drones communicating near the ground could potentially experience various paths of propagation due to the surrounding environment.
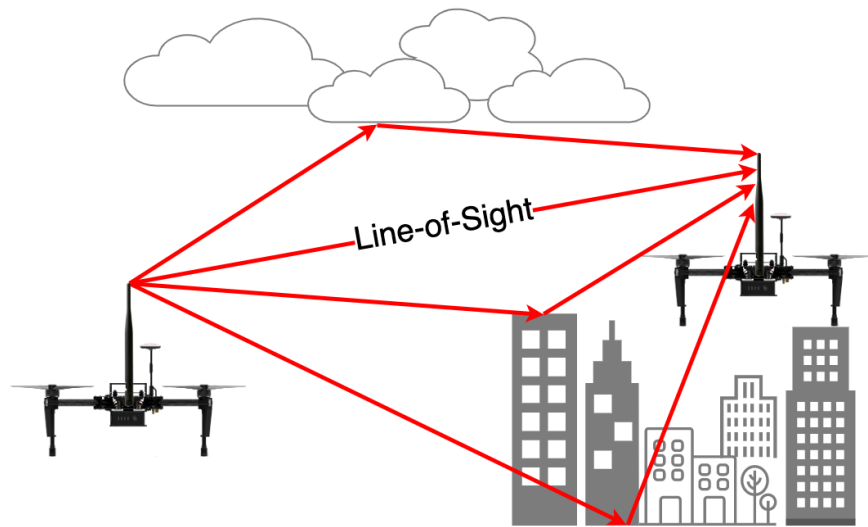
Figure 1.1: Multipath wireless propagation, including the line-of-sight component.

Even as these wireless signals travel near the speed of light, the combination of this multipath effect with the many unpredictable factors in the physical environment, such as a metal car driving by or a tree with all its leaves moving in the wind, can affect the quality of the signal. It is this unpredictable and uncountable number of factors that have some small effect on the wireless signal that adds up at the receiver and can cause the channel quality to vary. While in most instances we are concerned with the average quality of a wireless channel over time, if these effects are experienced extremely rapidly or over a long enough period, they can cause the wireless communication to fade to a point that it is no longer able to be understood by the intended receiver.

Within our drone studies, we focused on providing a detailed analysis of the three-dimensional aspects that are inherent to mobile drone platforms and their effect on wireless signal propagation in space. In particular, multi-rotor drones, or quadcopters, provide unique flight dynamics not typically seen with fixed-wing aircraft, such as jets or planes. Not only do multi-rotor drones have the ability to hover in place, but they can quickly change to any direction of travel in three-dimensional space. For our purposes, a three-dimensional Cartesian coordinate plane (X, Y, Z) is considered for describing a drone's position, while the orientation at that position is given by a form of Euler angles (roll, pitch, yaw) often associated with aircraft. Figure 1.2 illustrates the position and orientation planes on a drone body. Since a drone frame is a rigid body with fixed rotors, a drone modifies its position and orientation in space by applying various amounts of thrust to a corresponding combination of its rotors. Due to the weight/gravity experienced by a drone body with fixed rotors, a drone that is hovering in place can only modify its yaw orientation without affecting its position. If the pitch or roll is adjusted during a hover, this would result in movement in the X or Y plane. This unique ability of multi-rotor movements in all three-dimensions as well as the freedom to orientate in all 360 degrees of yaw provides drones with a unique perspective for wireless communication applications.

Furthermore, the majority of practical antennas don't produce a perfect sphere or isotropic, pattern of radiation for various reasons. First is a physical limitation. Since antennas are inherently passive elements, the connection, or termination with a wire to a radiation source unavoidably affects the radiation pattern. The second is for practical reasons. Most ground-based applications require coverage on the sides of the antenna, and not directly above or below. Since the amount of radiated power is so important for the quality of wireless communications, most antenna manufactures build the antennas in such a way that this power, that would otherwise be underutilized directly above or below the antenna, is directed towards the sides of the antenna.
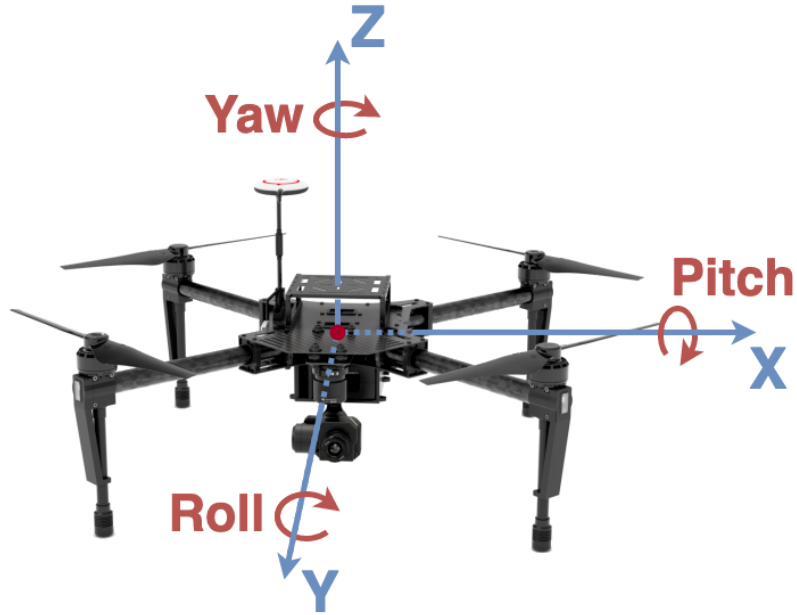
Figure 1.2: Three-dimensional illustration of the Cartesian coordinate plane along with their corresponding Euler angles. (DJI Matrice 100 [24])

For this reason, we chose to exploit this directional efficiency within our studies by using a common omnidirectional dipole antenna. This type of antenna produces a radiation pattern similar to the shape of a torus, or donut, perpendicularly to the plane that the antenna is vertically orientated in, as illustrated in Fig. 1.3. The greatest power density is experienced in the horizontal plane (X & Y) and the least power density is experienced directly above and below the antenna, or in the elevation plane (Z). Since power is such a precious resource on a mobile drone platform, we took this directional concept a step further by testing antennas in different positions and orientations to further explore how to create the best circumstances for providing an optimal wireless communication channel. By mounting antennas in various positions and orientations we can exploit the radiation pattern that is associated with this antenna by dynamically positioning or orientating the drone's frame.

As it became clear that the placement and orientation of the drone and antenna played a critical role in the communication channel, we sought to better characterize and isolate these complex three-dimensional effects. However, due to the dynamic outdoor environment
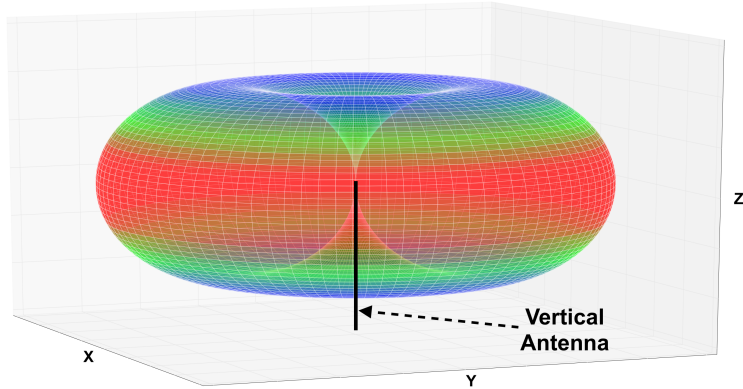
Figure 1.3: Three-dimensional torus like radiation pattern of a vertically orientated omni-directional dipole antenna.

in which we experimented, it became challenging to separate the influences of the environment from the drone induced effects and do so in an ongoing fashion. We focused on the physical antenna structure and how the antenna orientation/polarization (vertically or horizontally) could affect three-dimensional converge. Figure 1.4 provides a two-dimensional illustration of how the antenna pattern is affected in the elevation and azimuth plane depending on the physical orientation of the antenna. Notice that the elevation plane is rotated 90 degrees when the antenna is horizontally orientated, providing a greater radiated power density or gain in the positions above and below. To better understand the inherent characteristics of the radiation pattern in all three dimensions both on and off the drone, we performed experiments in an electromagnetically isolated environment known as a radio frequency anechoic chamber. This electromagnetic anechoic chamber is similar to that of an acoustic anechoic chamber, but instead of absorbing all sound, this chamber absorbs all electromagnetic radiation in the radio frequency range and mitigates the unintended wave propagation properties on the surrounding surfaces. This allows us to rotate the antenna 360 degrees in both the horizontal and vertical planes to measure the exact power received. These experiments provided insight into how the antenna pattern was affected while mounted on the drone, but the physical limitations of the size of the chamber didn't allow for in-flight testing or experimentation with more than one drone at once.
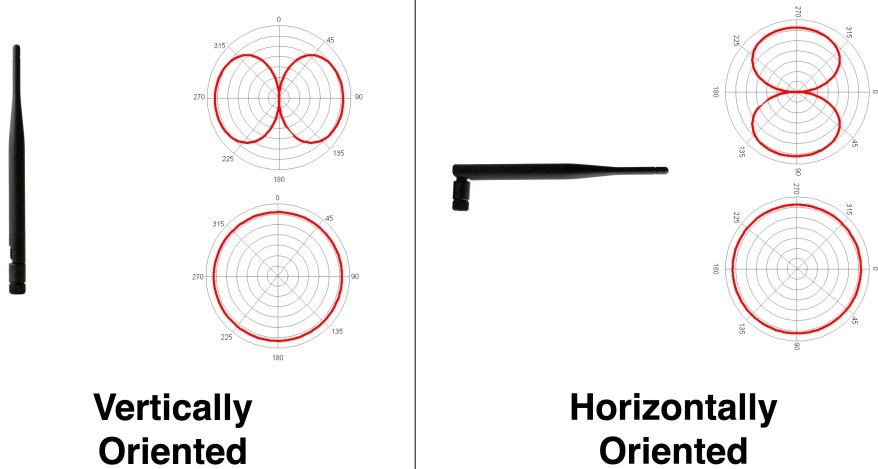
Figure 1.4: Two-dimensional representation of a vertically and horizontally orientated omni-directional dipole antenna, red line indicates (top) elevation plane cross section & (bottom) azimuth plane cross section.

As we developed a better understanding of how the antennas behaved on a drone platform for various communication scenarios, we wanted the ability to implement our developed empirical understanding with mathematical models for a computer-based simulation. In particular, modeling of the wireless behavior and drone-specific characteristics can be validated in a simulator using experimental measurements. Once the models are validated this enables the exploration of untested scenarios and applications. It also provides the ability to scale the number of drones to a level that would be impractical to implement in actual experimentation. This allows for the assessment of large scale coordination among complex multi-drone networks, or drone swarms. We explored the prospect of moving our single-drone in-field experiments and anechoic chamber knowledge to a simulation-based platform. A simulation environment can provide the ability to test network-level performance not currently feasible and better predict practical performance at scale. There already exist several works exploring drone-based simulators to provide a controlled and repeatable environment for understanding drone communications [25]. Some works focus on the dynamic nature that a mobile drone network experiences [26–28], while other works address more specialized aspects such as network security [29]. However, these simulation efforts tend to focus on

the link-level performance and provide a limited capability of modeling the highly detailed physical layer attributes, such as antenna characteristics, that can drastically alter standard models of wireless propagation and elevation effects. Attributes such as the physical drone body or the placement and orientation of antennas can have significant effects on the wireless propagation characteristics. However, these are typically modeled by a standard path loss or antenna elevation model. This led us in the direction of building a drone-flight-enabled isolation chamber to better characterize and begin to model these complex drone-specific wireless behaviors in a highly controlled environment.

We felt this path was necessary because taking measurements from a single drone was already a complex challenge. As our goal is to move from single-drone use cases to more than two drones coordinating at once, understanding the multidimensional nature from several drones while still maintaining the ability to separate the drone specific effects from the experimental variables became an impractical task. This was further complicated by the constantly changing outdoor environment and an increasing number of uncontrollable factors. It became clear that not only did we need an infrastructure capable of supporting several drones at once, but a way of providing a multidimensional understanding that can be separated from the drone body itself.

1.3. Contributions

In order to focus on the effects that are localized to the drone, we draw on the challenges we experienced with outdoor drone-based measurements to make informed design decisions. However, outdoor experimentation alone has several issues such as the lack of control of external factors that lead to unrepeatable effects and an inability to set up wireless measurement nodes to encompass a flyable space in an ongoing manner due to weather elements. While the anechoic chamber provides a highly isolated environment, it suffers from several limitations that prevent the assessment of multi-dimensional multi-drone networks. Hence, in this work, we design and build a drone-flight-enabled isolation chamber (Fig. 1.5) to

Figure 1.5: Indoor Drone-Flight-Enabled Isolation Chamber.

understand the spatial relationships that wireless drone links encounter. To carry out this vision, we address the following challenges with the described solutions:

System-Level Integration of Programmable and Observable Subsystems. First, we describe in detail the drone-flight-enabled wireless system and the experience that led to the specific indoor design. We explain the system-level integration of the infrastructure's supporting subsystems. We also describe the approach to addressing the challenges that an indoor system presents. While carrying out such an experiment, we additionally need to provide full observability of the drone platform and SDR network to facilitate a full view of the effects experienced by the drone.

Sending Drones to Fixed Positions for Fixed Time Durations. Without access to GPS, we seek to instruct a drone to fly to a certain indoor location and hold the position with high precision. As the precision level increases, the swarm scale can correspondingly increase. To do so, we give a detailed breakdown of the selected open-source drone platform that enables accurate control and coordination within the system. We show that proprietary solutions lack built-in solutions for highly-controlled positioning in an indoor environment and describe the integration of our open-source drone build with an 8-anchor indoor local-

ization system.

Synchronized Clocking and Logging across 72 Spatially-Distributed RF Chains.
Lack of GPS also impacts state-of-the-art solutions for controlling large-scale SDR networks.
Providing the same notion of time to 72 distributed nodes over 10s of meters required careful
considerations. Related to all of this, we analyze the challenges faced with the distributed
coordination of the various nodes. We then show the degree to which synchronization can
occur for the same experiment with first programmatic control and then post-processing.

Concurrent Wireless Capture from Various Horizontal and Vertical Positions.
To enable the greatest reach of our drone testbed to measure such effects as wireless signals
propagating to the receiver in various spatial paths known as multipath, or applications
such as using multiple antennas across different locations and independent systems known
as distributed beamforming, an extremely high sampling rate must be carried out at each
SDR. When 10s of SDRs are performing this measurement concurrently, a simple combining
of these data rates exceeds 2 Gigasamples/second (GS/s), which can overwhelm even very
high performing servers. Hence, we develop a distributed-server solution and evaluate the
extent to which these data capture rates can be maximized. We perform a highly-controlled
experiment to demonstrate the unique capability of the infrastructure.

Modeling Drone-Based Communications for Multi-Drone Networks. Finally, simulation-
based modeling of experimentally measured drone-based effects is demonstrated. As poten-
tial applications require an increasing number of drones across various three-dimensional po-
sitions and orientations, a programmable and scalable environment enables complex scenarios
to be evaluated. We demonstrate how drone induced effects can be accurately accounted
for in a network simulation tool. Lastly, we highlight the ability of the drone-flight-enabled
infrastructure to further validate developed models by isolating increasingly complex drone
specific characteristics for multi-drone networks.

Drone-Flight-Enabled Wireless Isolation Chamber

The goal of our drone-flight-enabled isolation chamber is to ultimately support a swarm of drones to fly at specified locations, whether fixed or mobile, for tens of minutes with a surrounding wireless infrastructure to monitor the wireless activity of that drone swarm. The extent to which the drone network can scale in the infrastructure heavily depends on the degree to which drones can be trusted to reliably hold position and the size of the space in which the flights can take place. The indoor drone-flight-enabled wireless isolation chamber is housed in an indoor facility that allows approximately 20x20 m of flyable space. The minimum height within the flyable space is 5 m along the perimeter of the flyable space, but the pitched roof along the center of the building allows a maximum height of 7 m. Surrounding this flyable space, safety netting is installed for the protection of personnel and SDR hardware.

In an indoor environment, accurate positioning is challenging, especially with a metal roof, as is the case in our facility. In fact, in Chapter 3, we even show that the interpretation of distances in an off-the-shelf drone controller from outdoor GPS in an unobstructed environment is to the extent that multiple drones flying inside a 20x20 m flyable space would be problematic. Also, the drone platform needs to be able to interpret position from a positioning system and be programmatic so that it can receive directives to move to a given position for a given amount of time. Both aspects have been elusive in a widely-used off-the-shelf system that we have used extensively for outdoor experimentation, motivating our custom design of an open-source drone platform.

Isolating and inspecting a single wireless event requires all 72 RF chains that are dispersed over a large three-dimensional cube to be temporally synchronized. In Chapter 4, we articulate the challenges of building such a network and evaluate the timing alignment of that network with a highly-controlled experiment in Chapter 5.

A final issue that we experienced in designing the drone-flight-enabled wireless isolation chamber has to do with the data sampling rate desired at each of the RF chains. Next-generation MIMO applications require an extended bandwidth [30–32]. To enable multi-path and MIMO phase-level analysis, each RF chain needs a sampling rate of at least 30 MS/s. With 72 RF chains, we need to record over 2.1 GS/s from all SDR positions. We explored the tradeoffs of distributed logging per SDR versus centralized logging and real-time versus post-experiment processing. In Section 4.2, we describe the details behind a surprising finding that a real-time, centralized approach greatly outperforms a distributed, off-line approach, which is due primarily to the design of the SDR.
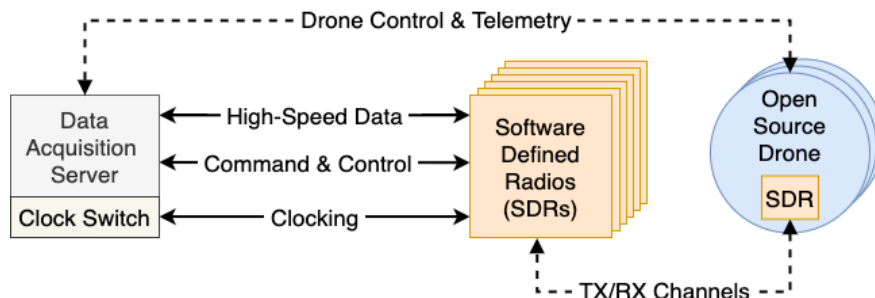
Figure 2.1: High-level overview of drone-flight-enabled wireless isolation chamber infrastructure.

In summary, the infrastructure relies on the following interacting subsystems: (*i.*) an indoor localization system due to the lack of GPS, (*ii.*) an open-source drone platform that directly interfaces with the localization system, (*iii.*) eighteen SDRs that are distributed along the walls and ceiling, which are each attached to four log-periodic antennas pointed toward the center of the facility and connected to each RF chain, (*iv.*) a five-server system for distributed data acquisition, and (*v.*) three dedicated cabling runs from each SDR to

the server rack for clocking (fiber), data logging (fiber), and control (Ethernet). The overall system infrastructure is illustrated as a block diagram in Fig. 2.1. Additionally, a 2D layout of the flyable space is shown in Fig. 2.2, pictured with an overhead view where the walls are laid down on the outside of the flyable space and each SDR is numbered with a surrounding square.
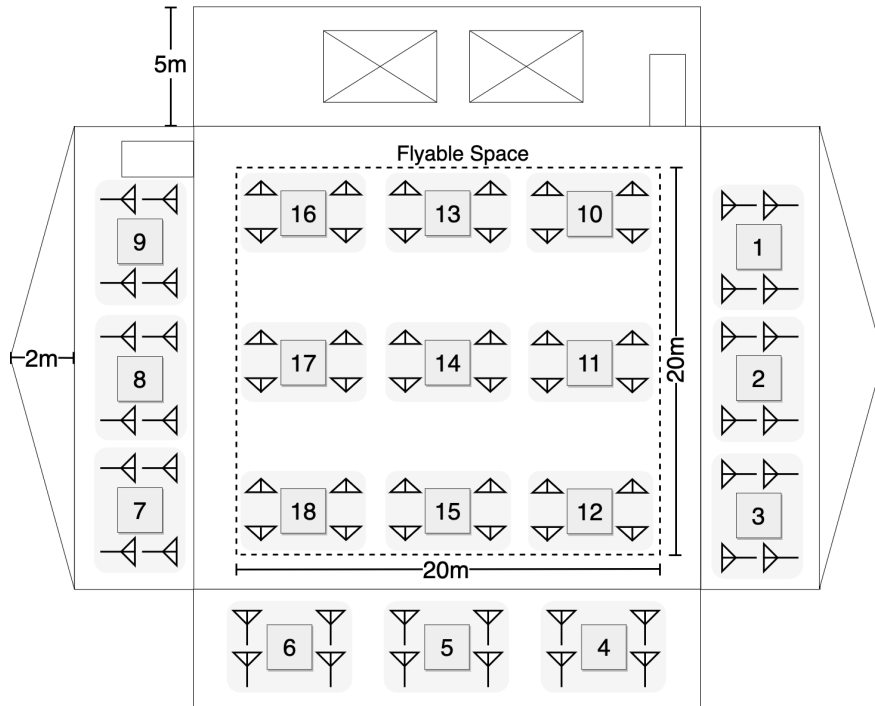
Figure 2.2: Layout of 18 - USRP N310s and 72 - Log Periodic Antennas.

Architecting an Open-Source Drone Platform

As mentioned previously, we have experience working with off-the-shelf proprietary platforms for a wide range of outdoor experiments. However, to accomplish seamless integration into our infrastructure we need more control over the software architecture and design as well as full visibility into the drone's flight control system. All of our efforts have been focused on multi-rotor drone platforms, more specifically quadcopters, that provide the ability to hover. This unique aspect of flight offers an unparalleled perspective for wireless applications. Designing a custom open-source drone platform with this capability took careful consideration of not only the flight dynamics and load capacity, but in the selection of open-source hardware and software to achieve our vision.

Even commercially engineered out-of-the-box drone platforms from established companies such as DJI suffer from errors in accuracy when attempting to hold a stable hovering position. According to DJI's specifications [24], their common Matrice 100 quadcopter platform's flight controller can have errors of ± 0.5 m in the vertical plane and ± 2.5 m in the horizontal plane when maintaining a hover under ideal flight conditions. These errors are only made worse in an unpredictable outdoor environment where several other factors can affect flight controller performance and accuracy. Factors such as wind, GPS error [33], and atmospheric fluctuations in temperature and air pressure can potentially induce unintended mobility and have a direct effect on the specified position and therefore the prediction and quality of a wireless channel. For example, one critical sensor that is responsible for introducing error in the vertical plane is the barometric air pressure sensor [34–36] associated with many consumer drone platforms, which does not have the ability to be calibrated. As the

14

atmospheric conditions fluctuate over time, this can greatly affect a drone's ability to hold or repeat a stable altitude.

For comparison, we demonstrate the accuracy of the popular DJI Matrice 100, a commercial load carrying drone-based on DJI's N1 flight controller. Fig. 3.1 illustrates the three-dimensional error experienced by the drone's intended hover position. There are a total of seven intended hover locations that are marked with a bold black point, and the measured GPS locations are indicated by the smaller blue points. The bounding circle indicates the intended position's corresponding measurements, while the dotted line indicates the distance from the intended point to the average of the received GPS measurements for that location. An external GPS receiver was used to separate the discrepancy that the drone's flight controller sensors experienced from the experimental measurements. From this outdoor experiment, we see errors of up to 3.57 m in the latitude axis, 1.53 m in the longitude axis, and 9.49 m in the vertical axis, or altitude, from the intended position when attempting to hover in a programmatically-specified location.
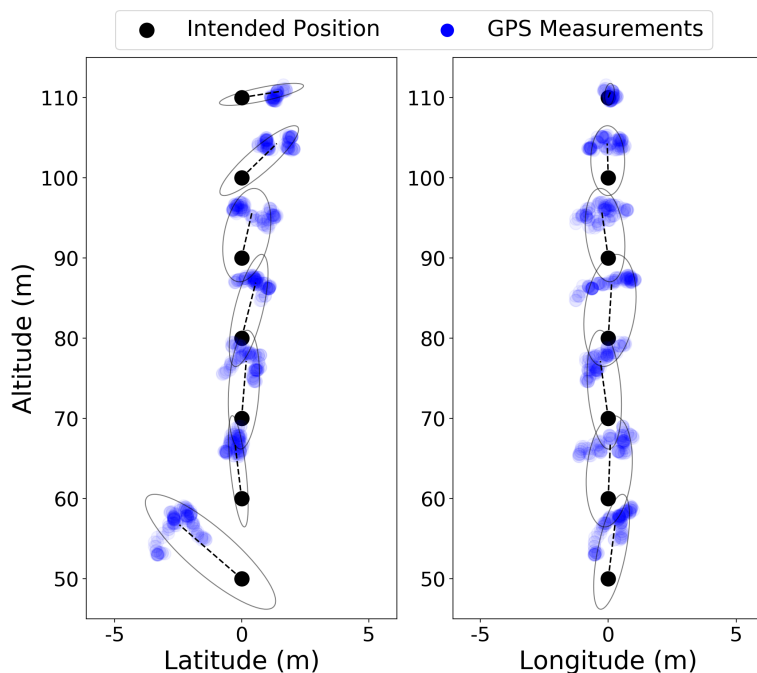
Figure 3.1: Error in latitude, longitude, and altitude from intended hover position.

15

Due to these DJI limitations for this indoor application, we began working with commercially-available, open-source drone platforms. We first used a 3DR Solo, which is based on the widely-used, open-source ArduPilot flight controller software and PixHawk Cube hardware. This platform supports a payload capacity of 700 g and is meant for more consumer-level hobby and photography applications. This drone was outfitted with the lightweight (24 g) Ettus USRP B200mini-i SDR for the wireless communication link and connected to a Raspberry Pi 3 Model B+ (RPi) for on-board processing. The RPi bridged the computing gap between the SDR and the flight controller over a serial data connection. Using the wireless SDR link, the RPi communicated received control messages to the flight controller and allowed flight sensor data to be transmitted to the ground station. The full-duplex capability of the SDR provided a frequency-division-duplex link that was needed to implement our custom communication protocol. The uplink channel was dedicated to critical drone control messages, and the downlink channel provided sensor feedback to the ground station. This separation of uplink and downlink channels enabled us to establish a functional SDR link to the drone and provide programmatic flight commands from the ground station based on sensor feedback.

Following our experience with the 3DR Solo, we continued to work with ArduPilot as well as PX4 for the flight control software and continued to rely on the RPi as the companion computing platform. We also continued using the PixHawk hardware as the flight controller interface on all of our subsequent drone builds. A total of three different custom drone platforms were built since using the 3DR Solo. The main difference between these platforms and the 3DR Solo is that the frame and motors were carefully selected to support a larger payload capacity ranging from 2 kg to our current platform's capacity of 6 kg, which is shown in Fig. 3.2. This increased capacity was necessary to support multiple radio platforms for control of the drone as well as provide separate wireless SDR links for use in dedicated experimentation. All of our custom open-source drones follow the basic design presented in

Fig. 3.3, with the exception of the indoor localization that was recently added for precise positioning inside the isolation chamber.
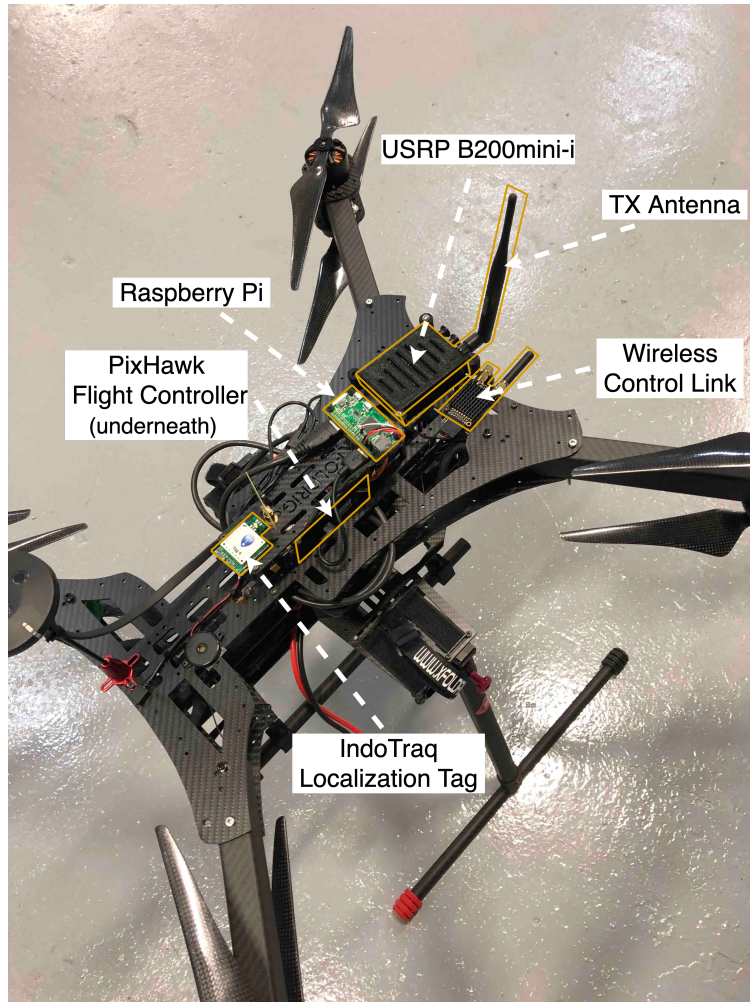
Figure 3.2: Open-Source Drone Platform.

In addition to the drone control method using an SDR link, there also exist several other options in terms of establishing a wireless control link to the drone, with varying degrees of reliability. Out of the various options we explored, the most common is a standard manual remote controller typically used for the purpose of hobby flight. This is not an ideal control method for repeatable and controlled experimentation, as even an experienced pilot would have trouble maintaining an accurate and precise level of repeatable position control. A GPS waypoint mission is another option, but this method is typically pre-programmed and offers no immediate feedback or dynamic control during the programmed flight mission.
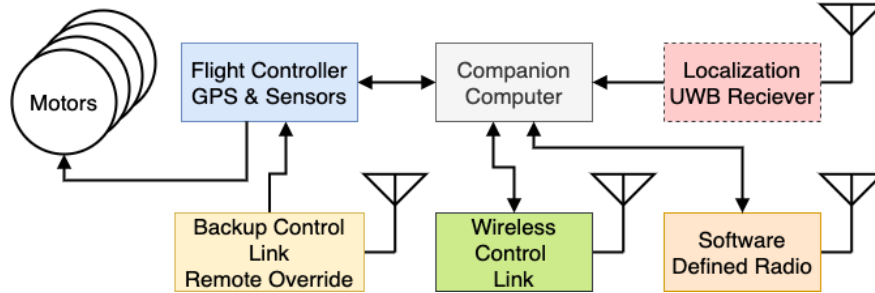
Figure 3.3: Block Diagram Design of Open-Source Drone Platform.

Another wireless control method that we explored used a standard 802.11 WiFi link to the companion computer. However, the performance of the consumer-level hardware caused excessive latency and reliability issues. Furthermore, all of these technologies, other than the SDR-based control links, are limited to their designed frequency bands, typically 900 MHz, 2.4 GHz, or 5 GHz bands. This would limit controlled experimentation within these popular frequency bands of interest. For this reason, an SDR-based control link is an attractive option as it allows for a dynamic selection of frequencies in order to stay out of the frequency bands where we wish to run experiments. It also provides the ability to structure control messages in any format, depending on the application. However, designing a robust protocol for an indoor environment to mitigate unique multipath and attenuation effects while maintaining low latency and desired baseband performance has been a challenge when using SDR hardware with limited computational resources. We physically steered control to the 3DR Solo while in flight to avoid equalization complexities in early SDR designs.

While an open-source drone platform provides the level of customization that we need to support highly-controlled experimentation with SDRs and interface the flight controller with our systems, these platforms require: (*i.*) meticulous considerations in the structural design and distribution of weight for good flight dynamics, (*ii.*) careful calibration of several sensitive sensors such as the compass, gyroscope, and accelerometer, and (*iii.*) manually incorporating any backup control and fail-safe features in case these sensitive systems have a

critical error or failure. In our design, a traditional remote control link is used as a fail-safe to take over manual control or issue an emergency motor stop in case of a critical error.

With the increased payload capacity that our custom drone platforms offer, other Linux development boards such as the Nvidia Jetson, ROCK960, and the MinnowBoard Turbot have been explored as a more powerful companion computing platform compared to the Raspberry Pi. These options leverage higher performance architectures that enable more robust processing power and an increased level of complexity onboard the drone. This enables the implementation of more intricate protocols and control schemes that are often optimized for different architectures (X86 vs. ARM). However, tailoring Linux (*e.g.*, OpenEmbedded) to meet the computational demands and dependencies of our system is an ongoing effort.

With the accuracy and precision of positioning within the three-dimensional (3D) space being so important for repeatable and controlled experimentation, an indoor localization method was needed. In order to achieve a detailed level of positioning within our indoor flight space, we installed a 3D position tracking system by IndoTraq. To do so, we secured tripods to the ceiling at each of the four corners of the flyable space to hold two anchors each at heights of 2 m and 4 m for a total of 8 anchors. This system uses ultra-wideband wireless technology in addition to inertial-based tracking to provide sub-millimeter precision with update rates as high as 150 Hz while also providing localization throughout the entire flyable space. In an 8 anchor system, accuracy in all three dimensions is within 16 mm of the intended position [37]. The ultra-wideband technology operates at a frequency of 6.5 GHz. This is outside the operable frequency range of our SDRs and therefore eliminates the risk of interference for isolated wireless measurements. A lightweight sensor tag (7 g) is integrated on our custom drone platform, pictured in Fig. 3.2, using a serial connection to the Raspberry Pi companion computer, and the calculated position is fed to the PixHawk flight controller in order to provide 3D positioning and tracking. Then, using the wireless control link, specified locations within the flight space can be programmatically and dynamically communicated to

the drone. This indoor localization solution along with the isolated indoor chamber addresses the previous GPS precision inaccuracies and atmospheric factors by eliminating the need to rely on the flight controller sensors that are prone to error.

Software Defined Radio Network for Distributed Data Acquisition

In this chapter, we describe challenges with the distributed SDR network mounted on the ceiling and walls around the flyable space: (*i.*) clocking over long distances, and (*ii.*) data logging from 72 RF chains.

4.1. Clocking Challenges with Distributed SDRs

The SDR platform used throughout the facility is the Ettus USRP N310. This SDR is capable of simultaneously providing four full-duplex channels (4 TX / 4 RX), each with a maximum instantaneous bandwidth of 100 MHz. It provides an extended frequency range of 10 MHz - 6 GHz and a sample rate of up to 153.6 MS/s. The N310 is a larger platform measuring 35.71 cm x 21.11 cm x 4.37 cm and weighing 3.13 kg, making it a challenge to fly on the drone. The SDRs that we have carried on the drone platform include the USRP B200mini-i and the USRP E312, weighing 24 g and 446 g, respectively. Both offer a tunable frequency range of 70 MHz - 6 GHz and provide up to 56 MHz of instantaneous bandwidth. The E312 offers two full-duplex channels, while the B200mini-i offers only one. The E312 possesses an embedded Linux system running on an ARM Cortex A9 chip enabling stand-alone operation, where the B200mini-i relies on a USB connection to a host. This makes the B200mini-i more suited for integrating drone control over an SDR link with a companion computer, while the E312 is more effective for collecting raw measurements or running a stand-alone protocol.

Each N310 has four LP0965 log-periodic PCB antennas connected to the RF front end that are operational over the entire operating carrier frequency range of the SDR. The 6-dBi antennas either point directly towards the floor from the ceiling mounts or directly towards

the opposing wall from the wall mounts. Each antenna connects to the TX/RX port allowing for time-division duplexing. With four antennas at each SDR, a total of 72 simultaneous channels can transmit, receive, or any combination of the two. Each of the eighteen SDRs has been strategically located to cover the flyable space with a 3-m spacing between adjacent antennas. Fig. 2.2 shows the arrangement of antennas and radios.

With so many radios operating together in a distributed fashion, a clocking solution was needed to provide synchronous operation. The first option explored was Ettus' Octo-Clock solution that provides synchronization for up to eight devices per OctoClock device. However, this solution is operated over copper connections and required a GPS input for a disciplined clock source. These factors proved challenging for several reasons. First, the max distance from the central clock source would be approximately 30 m away when the cables were routed. This is not practical for copper-based connections as these distances would experience significant cable losses as well as introduce unnecessary drift and noise in the clock pulses, resulting in unacceptable errors in synchronization. Secondly, the indoor environment lacked a reliable GPS signal which would further degrade the quality of the clock source. The clocking method that we chose to incorporate in our system was the White Rabbit Network Switch from Seven Solutions. This solution provided sub-nanosecond time accuracy over fiber connection for up to eighteen devices on one network switch. Since it operates over a fiber link, it can support multiple-km distances, easily supporting our needs. It also didn't require a disciplined clock and still offers a clocking accuracy to within 1 nanosecond [38]. Using the White Rabbit clock, we ran single-mode fiber cable from a central control point to each of the eighteen radios to provide accurate and distributed clocking, which we experimentally evaluate in Chapter 5.

4.2. Challenges to Command/Log 72 RF Chains

Another critical challenge faced with operating eighteen SDRs in such a distributed fashion is providing command and control to each radio. The other challenge that logically followed

was collecting, generating, and processing the large amount of data that would either need to be created or captured at each radio. First, to provide remote command and control, a wired 1 Gbps Ethernet-based connection was established to each of the radios. This allowed for remote configuration from a central point but didn't provide a method for collecting, processing, or storing measurement data. To address this we took a methodical approach in assessing different techniques for handling this challenge.

We first explored processing samples locally at each N310. However, each radio was limited to the local ARM Cortex-A9 processor and used a flash-based microSD card for data storage. Using a single N310 to benchmark a radio's performance, first, the Unix command-line utility 'dd' was used to test the disk write speed in MB/s for several different microSD cards from various manufactures. Next, based on the max disk performance, a theoretical sample rate was calculated to predict the max achievable sample rate. This calculation was based on the fact that each sample written to file is a complex float producing a total of 8 bytes per sample or 4 bytes per I and Q, respectively. Finally, the true measurement capability was assessed by using a benchmark utility provided by Ettus and slowly backing off the predicted sample rates until there was no longer data overflow, meaning loss of samples due to the lack of buffer space. Each microSD card's speed class, capacity, quoted write speed, 'dd' write speed results, calculated theoretical max rate, and benchmark utility test results were recorded. The results from these tests are presented in Table 4.1. From these results, we show that the max sample rate achieved was approximately 1.5 MS/s, greatly underutilizing the N310's max capability of 153.6 MS/s.

Next, we shifted from locally-processing samples to attempting to send and receive samples using a networked mode. To achieve this process and handle the large amount of data associated with higher sample rates, we identified the need for a high-performance computing platform. To better understand the computing needs and data rate budget, we started with one server-grade machine to test how many radios we could support on a single machine

Card	Class	Capacity (GB)	Write (MB/s)	'dd' (MB/s)	Max Rate (MS/s)	Tested Rate (MS/s)
Samsung Evo	10, U3	512	90	17.5	2.1875	1
Samsung Evo	10, U3	256	90	15.6	1.95	1.201923
SanDisk Extreme	U3, V30	400	90	17	2.125	1.506024
SanDisk Extreme	U3, V30	128	90	17.2	2.15	1.404494
Lexar Professional	U3, V90	128	150	10.9	1.3625	0.5

Table 4.1: Write and sample rate performance of microSD cards.

before scaling to a multi-server setup to service all eighteen radios. We used a dedicated quad-port SFP+ network interface card (NIC) operating on Peripheral Component Interconnect express Revision 3 (PCIe Rev. 3) to provide a direct link from the N310 to the server to get the best data rate and network performance without any potential bottlenecks in the network, such as a router or switch.

The first cabling method tested from the N310 to the server was CAT 6 RJ45 Ethernet, supporting 10 Gbps on an SFP+ adapter at both the radio and NIC. However, when testing the max distance cable length of 30 m, the link did not support the full 10 Gbps speed and reverted to a 1 Gbps link. Since this issue would bottleneck the data link budget, we then moved to using a full-duplex multi-mode fiber connection over a supporting SFP+ adapter at both the radio and NIC. With the full 10 Gbps speed in both the uplink and downlink confirmed, several tests using a network-mode benchmark utility allowed us to gauge how many radios we could support using one machine. Using up to three quad-port NICs on the single server-grade test machine, we benchmarked the performance for a total of 4, 6, and 9 network-mode links with the radio front end connection configuration, set receiver (RX) sample rate, and set transmitter (TX) sample rate noted. Then, each test was performed for 10 s.

The results for the various tested combinations of receiving RX and generating TX sample rates are shown in Table 4.2. The front end connections refer to the number of front end connections per radio, so 4-RX and 4-TX across four N310s signify a total of 16 channels of

both RX and TX. The tests that completed without an underflow or overflow in the network buffers are indicated with a pass (P), where those that experienced at least one buffer issue are indicated with a fail (F). These front end combinations were selected to assess the best and worst-case scenarios for different configurations. From these results, we conclude that connecting four radios per machine in the server design would provide the best network performance for processing samples and still achieve near the maximum capability of the N310 hardware.

Therefore, a total of five servers were custom built to match the specifications of the test machine and provide dedicated connectivity to each of the eighteen SDRs. Each server was outfitted with one quad-port NIC, 2 terabytes (TB) of high-speed solid-state storage (2 x 1 TB in RAID 0) with a maximum write speed of 3.3 GB/s, and 10 TB of hard disk space that allows offloading from high-speed storage to enable various combinations of collection times and sample rates. An overview of the clocking and server system architecture with connections to each N310 is presented in Fig. 4.1.

$$Data\ Rate(DR) = Sample\ Rate(SR) \times 8\ Bytes \times \#\ Channels(C) \tag{4.1}$$

$$Collection\ Time(CT) = \frac{Disk\ Space}{Data\ Rate} \tag{4.2}$$

$$E.g.\ SR = 30MS/s,\ C = 16,\ DR = 3.84GB/s,\ CT = 520.8\ s$$

Equations 4.1 & 4.2 demonstrate the theoretical maximum collection time based on the sample rate and number of channels. Recall, each server has a maximum of four connected N310s and therefore, a maximum of 16 channels per server. Using the high-speed 2 TB

storage and sample rates of 30 MS/s across all 16 RX channels for one server results in a maximum collection time of 520.8 s.
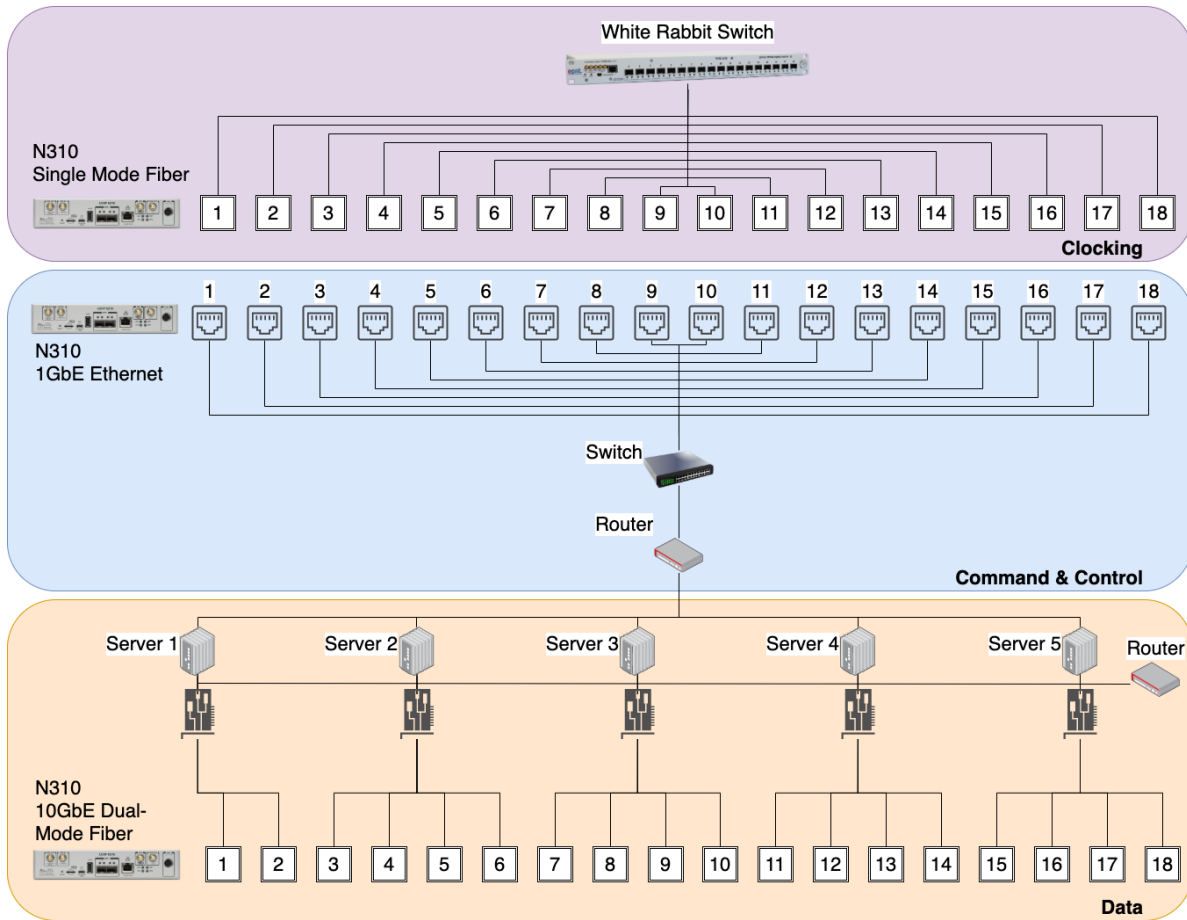
Figure 4.1: Detailed overview of clocking, command & control, and data acquisition server system layout.

Front End	RX (MS/s)	TX (MS/s)	Pass/Fail
Four - N310			
1-RX	125	N/A	P
1-RX	125	N/A	P
1-RX 1-TX	125	125	P
1-RX 1-TX	125	125	P
4-RX 4-TX	62.5	62.5	P
4-RX 4-TX	62.5	62.5	P
4-RX 4-TX	125	62.5	F
Six - N310			
1-RX	62.5	N/A	P
1-RX	125	N/A	P
4-RX	31.25	N/A	P
4-RX	62.5	N/A	F
4-RX	125	N/A	F
1-RX 1-TX	62.5	6.25	P
1-RX 1-TX	62.5	12.5	F
4-RX 4-TX	31.25	1.25	P
4-RX 4-TX	62.5	1.25	F
4-RX 4-TX	12.5	6.25	F
4-RX 4-TX	31.25	6.25	F
Nine - N310			
1-RX	20.83	N/A	P
1-RX	31.25	N/A	P
1-RX	62.5	N/A	F
4-RX 4-TX	1.25	1.25	P
4-RX 4-TX	31.25	31.25	F

Table 4.2: Achievable sample rates in networked mode based on number of SDRs connected to a single server.

CHAPTER 5

Multi-Dimensional Wireless Data Capture Results

To demonstrate the scale and level of control at which we can perform experiments, we provide a simple experimental setup for capturing received samples from a transmitting drone. First, to achieve a distributed level of control, the servers institute a parallel control scheme that issues command messages over the Ethernet network and directs each USRP to their respective server over fiber to start a measurement collection. Using Ettus' USRP Hardware Driver (UHD) software API, a simple write-to-file application is created to sample 1.25 MHz of bandwidth at a center frequency of 5.15 GHz. For this demonstration, we capture one RX channel across all eighteen SDRs simultaneously. To isolate the effect of receiving from each location, the drone is placed on a fixed platform at the center of the flyable space directly below SDR #14 in Fig. 5.2 at a height of 3.5 m. The drone is orientated with an omnidirectional, vertically-orientated TX antenna in Fig. 3.2 facing towards SDR #2. The USRP B200mini-i SDR is used as the transmitter on the drone and sends a narrow-band sine wave at a center frequency of 5.15 GHz in a periodic on-off pattern with a cycle frequency of 0.5 Hz. Then, one receiver chain from each of the eighteen N310s simultaneously samples at a rate of 1.25 MS/s for a total of 30 seconds. The IQ samples are stored from each SDR on their respective server and are later processed for the received signal strength (RSS) in dB.

Fig. 5.1 shows a one-second portion of the transmitter-on cycle for a temporal representation of the RSS. To better visualize the general trend, a moving average was taken over a window size of 3000 samples. The top graph shows the best synchronization that can be achieved with programmatic control alignment of sampled data by using a timestamp from

the start of the collection. While the bottom graph shows the post-processed alignment, based on the rising edge of the first cycle. There was a maximum of 26,907 samples, or 21.53 milliseconds, between the first and last rising edge using the programmatic control method of synchronization. After post-processing based on the rising edge, both the rising and falling edges were perfectly aligned.
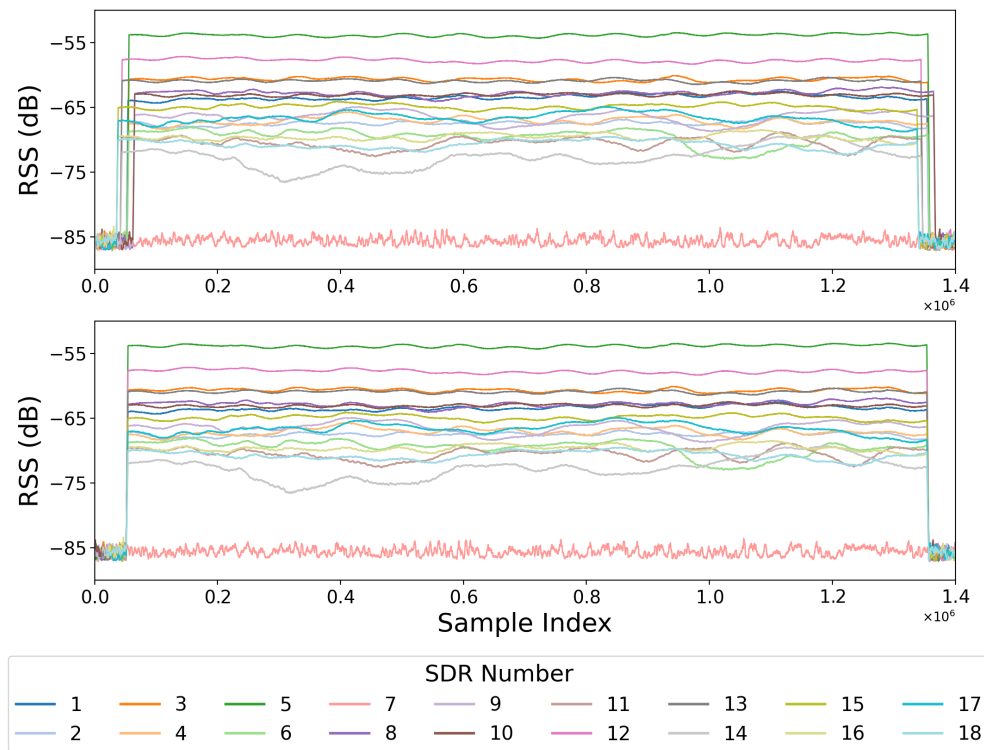
Figure 5.1: Average RSS with programmatic (top) and post-processed (bottom) synchronization.

By inspecting the RSS values in Fig. 5.1, we see a maximum of a 23.12 dB difference in the RSS from SDR #14 to SDR #5, across all eighteen spatially-distributed receivers. We can additionally refer to Fig. 5.2, which illustrates the overall average RSS experienced at each SDR in the form of a colored heat-map overlay. Both of these figures indicate that the drone experiences vastly different propagation effects from approximately equidistant receivers in this controlled environment. In particular, the receivers located above the drone are consistently lower in terms of their received signal quality as compared to the antennas on the walls, likely due to the transmitting, vertically-oriented omnidirectional antenna which

29
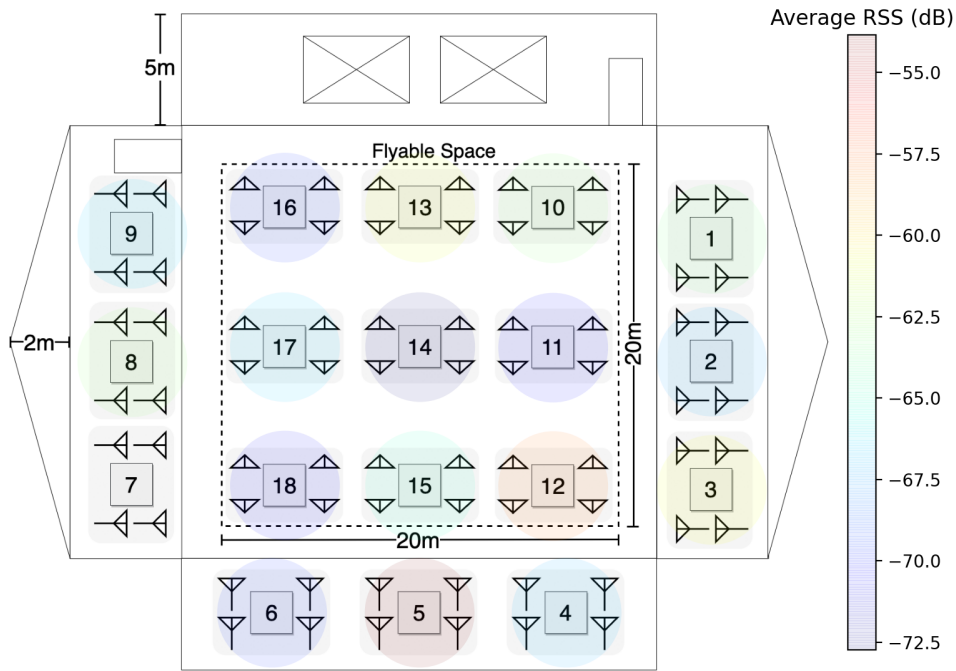
Figure 5.2: Layout view of average RSS highlighted from measurement results.

has the lowest radiation pattern value at that elevation angle. Furthermore, there is diversity even among the walls, highlighting the potential impact the drone body itself is having on the *omnidirectional* antenna mounted on the SDR #2 side of the drone. This further highlights the need to better understand the complex three-dimensional effects that drones experience, a key component that our unique drone-flight-enabled wireless isolation chamber enables.

CHAPTER 6

Building a Drone-Based Simulation Environment

Our work towards a drone-based simulation environment focuses on modeling our experimental understanding and implementing those results in a computational setting. In particular, an emphasis is placed on emulating the physical layer characteristics that we have identified and accurately representing their impact on the wireless channel. Compared to standard wireless propagation and elevation models, our experimental results show an increased need for characterizing multi-dimensional drone specific aspects to properly represent practical drone-based communications. Aspects such as the relative three-dimensional location of drone nodes, the physical drone body, placement of antennas, and orientation of the antennas require several variations in standard models to effectively represent their induced effects. Properly capturing and representing these effects becomes increasingly important as the scale of the drone network increases. By accurately modeling the multi-dimensional characteristics, we can predict the complex communication channels among large networks of drones across diverse three-dimensional positions and altitudes.

Rather than programming a custom simulation environment from the ground up, we chose to utilize an existing network simulation tool. There exist several software-based network simulators such as NS-3, OpNet, and NetSim that can provide a starting point for mobile ad hoc networks. We chose to use OMNeT++ with INET, a C++ based framework that provides several models that can easily be customized to represent the required elements of multi-dimensional drone-based communications. In particular, we needed a programmable environment to simulate a complex network stack, implement several physical layer aspects, create various wireless interfaces, provide three-dimensional mobility, and assess radio and

network-level performance. OMNeT++ with INET provided a sufficient starting point for all of these requirements.

In our initial simulation work, we have demonstrated how experimental results from our outdoor measurement studies and indoor anechoic chamber experiments can be transferred to a simulation environment for the evaluation and validation of drone-based communications. In particular, we have explored two-dimensional and three-dimensional scenarios that have taken into account the effect of the drone body as well as multiple antenna orientations and positions. It is important to note that to effectively target the drone induced effects, all of the described experiments utilized the same antenna across similar frequencies eliminating any physical antenna dependent characteristics when comparing results. However, as previously mentioned we lacked an isolated control of other variables in the outdoor environment to completely separate the various undesirable effects from the intended experimental variables. Even in the isolated environment of the anechoic chamber, there are limitations that prevent the characterization of altitude effects, in-flight effects, and the assessment of multiple drones at once. Regardless of these barriers, we have gained valuable insight into how our developed models can accurately predict observed wireless behavior in a simulation-based environment. This initial step brings us closer to providing a repeatable and scalable simulation framework to accurately describe complex multi-drone networks.

Our initial transfer of an experimental model to the simulation environment focused on a simple two-dimensional representation of the relative angle between a transmitting drone to a receiving drone in an outdoor, unobstructed line-of-sight environment. The general layout and results from this in-field experiment are represented in Figs. 6.1 & 6.2. An important aspect of this experiment is that both drones were fixed at the same elevation and had their forward-mounted antennas facing towards 0 degrees (fixed yaw) throughout this experiment, creating a unique scenario for assessing two-dimensional directional losses. Figure 6.1 illustrates the distances and angles that were measured with the receiving drone

in the middle and the transmit drone positions highlighted with the average received signal strength (RSS) experienced by the receiving drone along each axis creating angles of 0, 90, 180, and 270 degrees. From this figure, it is clear that the transmitting drone that was directly in front of the receiving drone provided the highest RSS of the measured angles.
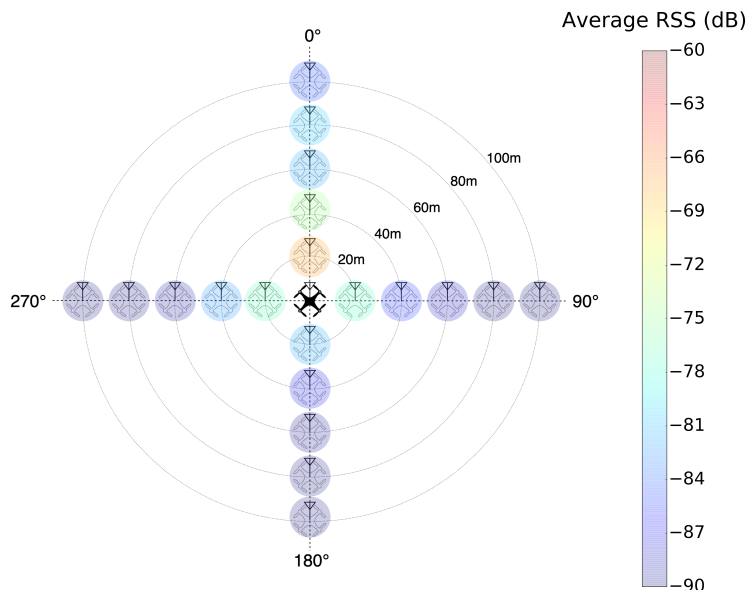
Figure 6.1: In-field two-dimensional experiment RX drone (center) with TX drone positions (surrounding), average RSS highlighted.

It is common to assume that in a fixed horizontal, or azimuth plane that the radiation pattern and therefore observed losses would be constant no matter the direction of the transmitter from the receiver. However, from our two-dimensional experiment it was clear that once the antenna was mounted on the drone and the transmit-receive angle was changed, this assumption was no longer valid. Figure 6.2 shows a detailed plot of the RSS for each measured angle and distance (20, 40, 60, 80, 100 m). The dotted line illustrates the predicted RSS using a standard log-normal path loss model. Using this standard path loss model, we observe that a constant azimuth assumption greatly underestimates the path loss experienced by the drone by up to 23.15 dB. To account for these losses, we represent the differences in path loss by adding a shadowing factor to a log-normal path loss model for each of the measured angles. This modified model allowed us to accurately predict and simulate the

RSS for each measured angle. This modified model produced a maximum average prediction error of 4.10 dB in simulation for the angle of 180 degrees. When compared to the standard model error of up to 25.58 dB, we demonstrate an 83.9% reduction in error.
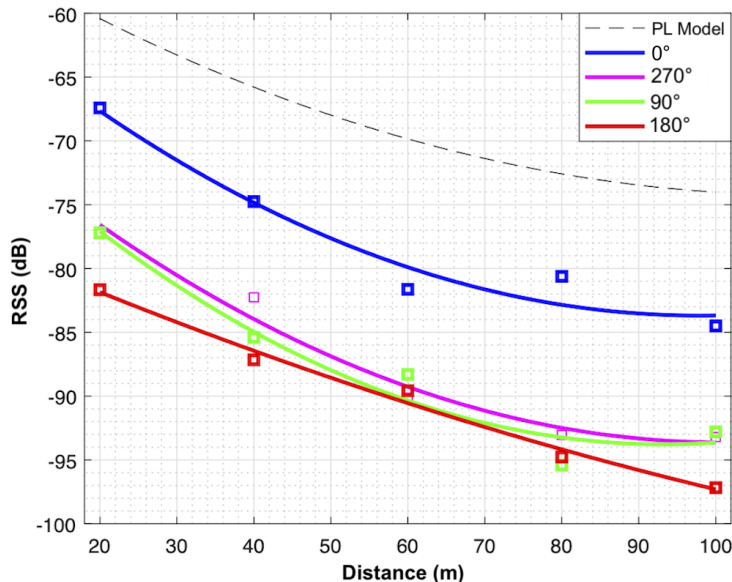
Figure 6.2: In-field RSS vs. Distance for each measured angle, predicted standard path loss model also shown (dotted line).

To simulate this experiment within OMNeT++, an ad hoc drone network was created to match the experimental setup and parameters. An existing wireless AdhocHost module was used to represent the transmitting and receiving drones. Then an Ieee80211ScalarRadioMedium module was used to simulate the wireless physical layer parameters. Within this module, an omnidirectional dipole antenna was chosen to match the in-field experiment antenna characteristics. Next, an Ipv4NetworkConfigurator module was used to assign IP addresses and create the routing between network interfaces. Finally, to implement our modified path loss model, a custom module was created in C++ to capture the relative transmit-receive angle and calculate the corresponding path loss based on the added shadowing factor. This calculation was done using a lookup table and was only valid for the four distinct angles that were measured.

Equations 6.1 & 6.2 summarize the modified path loss model that was used for this calculation. In Equ. 6.1, the transmit power and receive power are represented by P_t and P_r respectively. Then $P_L(d_o)$ is the reference path loss calculation for a distance of 20m, α is the path loss exponent, and ξ_s is the zero-mean, normally distributed shadowing parameter with a standard deviation of 2. In Equ. 6.2, PL_{UAV} represents our modified path loss value where Γ_ϕ is the additional averaged shadowing parameter that was induced by the drone in the corresponding azimuth angle (ϕ). To produce an accurate calculation within the simulation, the same center frequency (2.5 GHz) and transmit power (6.2 dBm or 4.1687 mW) parameters were matched. Finally, the simulation was run at 1 m increments from a distance of 20 m to 100 m while the received power was logged at each location.

$$P_r = P_t - P_{L(d_o)} - 10\alpha log(d/d_o) + \xi_s \tag{6.1}$$

$$PL_{UAV} = PL_{log-distance} + \Gamma_\phi \tag{6.2}$$

Figure 6.3 shows the simulated results using our developed model for the angles of 0 and 180 degrees, or an additional shadowing factor (Γ_ϕ) of 9.17 dB and 21.45 dB respectively. When compared to the in-field experiments where only five distances were used to develop the model, we show that on average, the same accuracy is achieved in distance increments of 1 m.

While this two-dimensional path loss model highlighted the substantial effect that the drone body had on predicting RSS, it did not capture all 360 degrees of yaw or the various complex antenna positions and orientations that we wished to simulate on a larger scale. It also didn't provide a means of separating the drone induced effects from the drone-based transmitter. Furthermore, this experiment failed to describe the unique three-dimensional angles that drones experience when operating at different altitudes, a key aspect of drone-based communications.
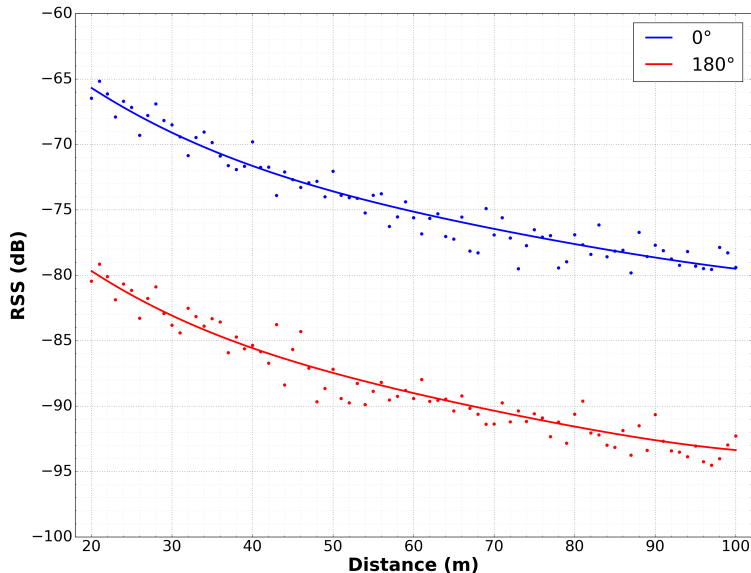
Figure 6.3: Simulated RSS for 0 & 180 degrees with distance increments of 1 m.

Once we identified that the drone body was a substantial source of attenuation, we shifted focus from a path loss based model to characterizing the attenuation using a directional gain based approach. A gained based approach to modeling the unique drone-based aspects allowed us to assess how the directivity of the wireless signal is affected from the perspective of the antenna by the complex influence of the drone body as well as the various antenna positions and orientations. This approach also allows for the simulation environment to be easily extensible to various drone bodies and antenna configurations by simply characterizing a specific drone and antenna setup once and scaling to any physical network topology necessary. This shift in modeling was chosen because path loss is typically associated with characterizing the surrounding propagation environment and not the direct effect of the drone body or the characteristics induced on the communicating antennas. It also allows for the logical separation of transmitting and receiving elements and their induced effects when evaluating drone-to-drone networks with various antenna configurations. Since our outdoor experiments were performed at an altitude where unobstructed line-of-sight propagation was assumed, the concept of path loss did not completely capture the observed effects that the drone had on RSS.

Following this realization, we utilized the anechoic chamber to characterize the antenna gain in great detail both on and off the drone in a highly isolated manner. Again, due to the limited capabilities of the chamber, we were only able to accurately describe the yaw dimension, or azimuth plane, of the antenna for a vertical antenna orientation. Within the anechoic chamber, we characterized the antenna without the drone as well as for two different positions on the drone. The controlled nature of the chamber enabled us to capture a greater level of detail about each antenna configuration in the azimuth plane. Figure 6.4 shows the setup within the anechoic chamber and two antenna positions measured on the drone body. The drone was mounted on a rotating platform controlled by a stepper motor with a resolution of 1.8 degrees. This provided a total of 200 individual antenna gain measurements for each antenna configuration.

Using this highly detailed characterization of the gain pattern experienced by the antenna, the same in-field experiment was recreated in the simulation environment. However, now we were able to provide a full representation of the azimuth plane both with and without the drone body for all 360 degrees of yaw and the same experimental distances. Within OMNeT, the same basic drone network setup was used as in the previous simulation. However, this time instead of a dipole antenna, the transmitting and receiving drones were configured with an interpolating antenna that models a directional antenna based on a sequence of angles and gain values. Using the 200 angles and gain values measured in the chamber, these antennas were set up to match the exact characterization for each antenna configuration. The normalized gain values for each of the three configurations measured are illustrated in Fig. 6.5. The three configurations are: (a) the antenna isolated on its own, (b) the vertically drone-mounted position 1, and (c) the vertically drone-mounted position 2. Again, the same transmit power and center frequency was matched, but this time a free-space path loss model was used rather than the modified log-normal path loss model.

By comparing these antenna gain patterns, we can see that the isolated antenna produces a fairly symmetric gain pattern in the azimuth plane. However, compared to the two drone-mounted antenna positions, it is clear that the drone induced a substantial effect on the antenna gain pattern. While several angles achieve a similar gain as the isolated antenna, other angles show substantial losses due to the drone body. These differences in the effective gain pattern will ultimately affect the performance of the wireless channel depending on the transmit-receive angles produced and need to be accounted for to properly model multi-drone networks where any combination of angles is possible.
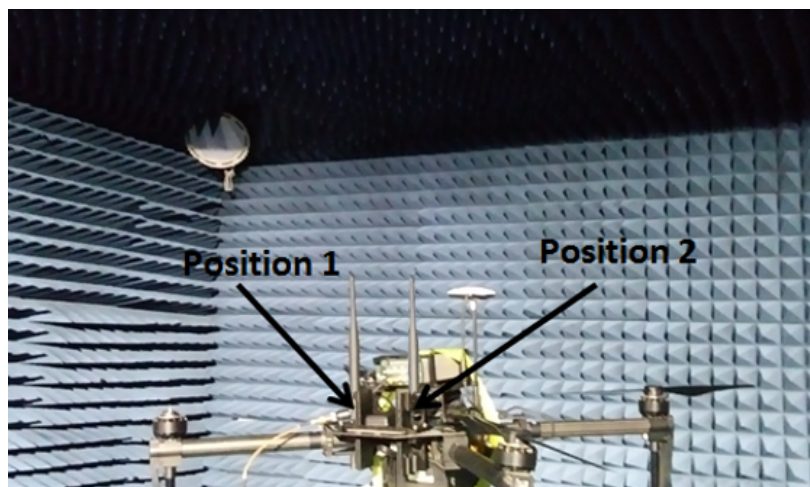
Figure 6.4: Anechoic chamber measurement setup with two antenna positions.

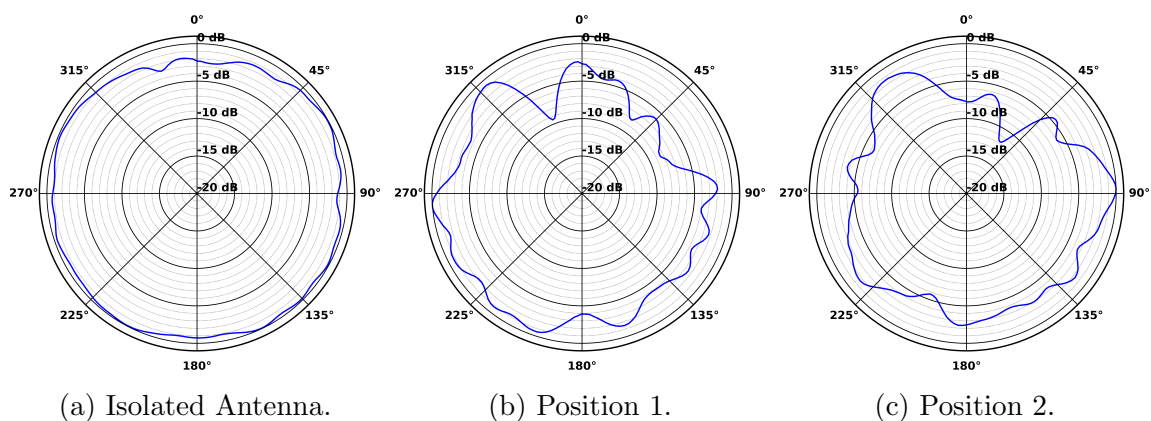(a) Isolated Antenna.   (b) Position 1.   (c) Position 2.

Figure 6.5: Measured antenna gain pattern for isolated & drone mounted antenna.

By leveraging this detailed understanding of the effective antenna gain patterns, we illustrate the impact that the drone body has within the simulation environment. Figure 6.6

provides a heat map representation of the predicted RSS for all three antenna configurations across the same distances as our in-field experiments. The color map key represents the expected RSS in dB experienced by the receiving drone at the center from each of the surrounding transmit locations with a 1 m resolution. As expected, the isolated antenna shows a gain pattern in the azimuth plane that is characteristic of a vertically orientated omnidirectional dipole antenna. Compared to the isolated antenna configuration pattern, it is clear that the drone has a significant effect on the achievable gain of the antenna and therefore the RSS performance for different transmit-receive angles and distances.

Even with the same drone-mounted antenna orientations and similar positions (Fig. 6.4), there exist differences in the induced azimuth gain patterns represented in Figs. 6.6b & 6.6c, further highlighting the need to carefully characterize the various antenna orientations and placements on the drone. One interesting observation from these figures is that the forward-facing angle opposite of the receiving antenna placement experiences substantial losses (dark-blue cone pattern) starting at 40 m centered at approximately 335 and 35 degrees for position 1 (Fig. 6.6b) and position 2 (Fig. 6.6c) respectively. These observations are important when predicting the effective distance and channel quality as these losses will limit the potential range and/or achievable throughput for those specific angles.

In our later outdoor experiments, we went on to characterize how altitude affected RSS for various three-dimensional drone positions and antenna orientations. In these experiments, we again used two drones at a sufficiently high altitude to assume free space line-of-sight propagation, but this time we focused on the receiving antenna orientation as well as the three-dimensional position and consequently the angles they created. It is important to note that because of the altitude chosen to perform these experiments, the transmitter had to be mounted on a second drone introducing a drone-based elevation plane effect that has not been characterized or accounted for. Regardless, in this experiment, the transmitting drone was fixed and the receiving drone flew around and took measurements while hovering. Figure

(a) Isolated Antenna.
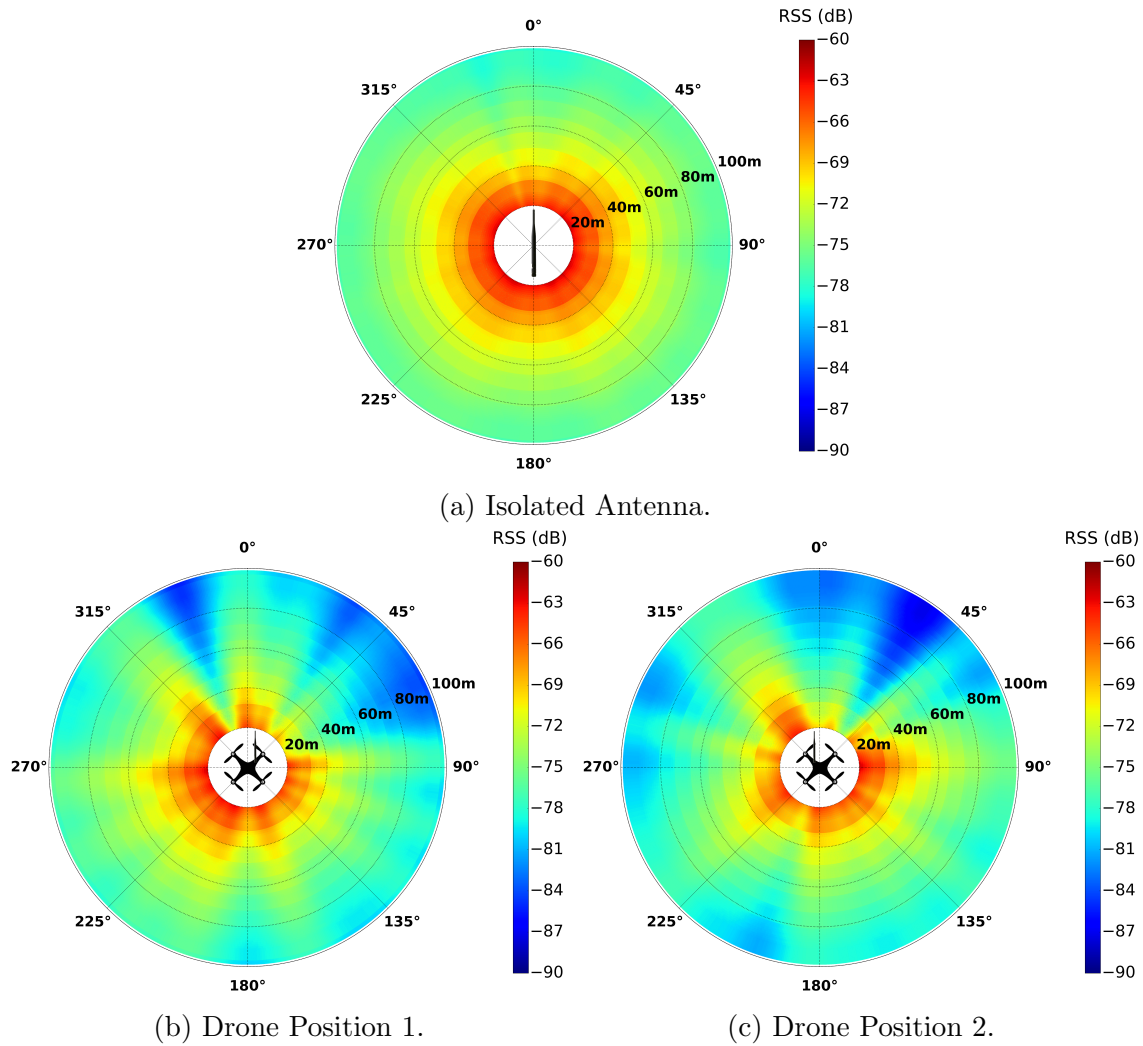

(b) Drone Position 1.

(c) Drone Position 2.

Figure 6.6: Simulation results of gain pattern for isolated & drone mounted antenna.

6.7 illustrates the experiment setup and averaged RSS results for the three receive antenna orientations (vertical up, vertical down, and horizontal) and nine different drone positions and their corresponding angles. The black drone symbol represents the transmitting drone where the transmit antenna was orientated vertically up on the forward center of the drone body throughout each experiment. This was done to represent an ideal transmitter as best as possible to characterize each corresponding receiver orientation. For the positions not directly above or below the transmitting drone, a horizontal separation distance of 20 m was used for those seven locations (to the right of the transmitter in Fig. 6.7). The average RSS is highlighted in the form of a color map for each of these experiments to illustrate

the differences that these three receive antenna orientations induced on the various three-dimensional positions and angles. We observed a substantial dependence on the relative three-dimensional angles and antenna gain pattern based on the receiving antenna orientation during these in-field experiments.
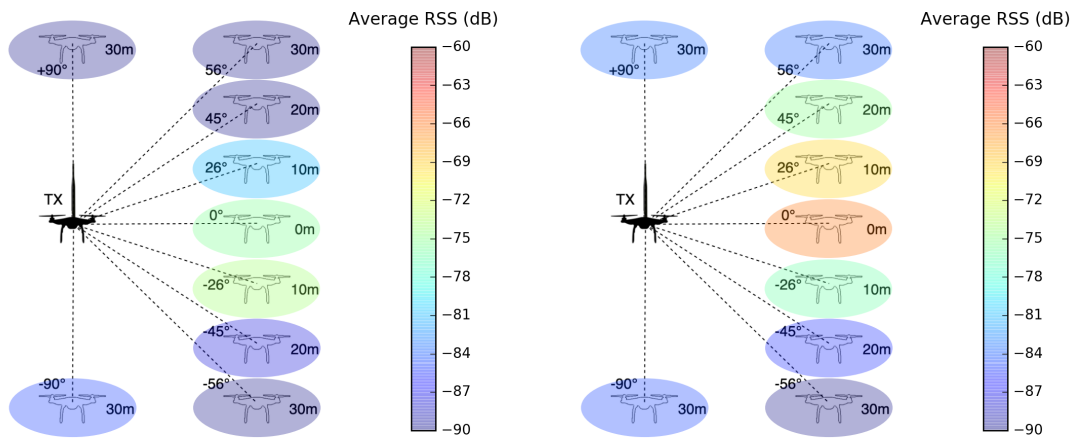
(a) Vertical Up Receiving Antenna.

(b) Vertical Down Receiving Antenna.
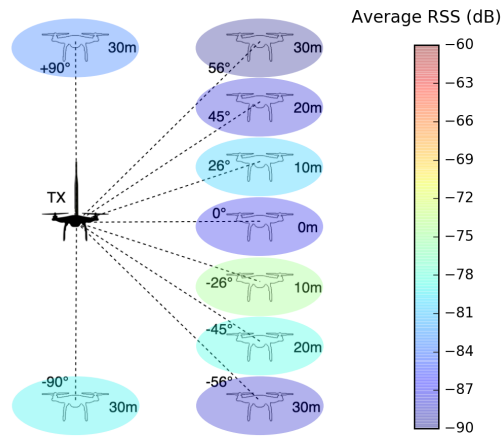
(c) Horizontal Receiving Antenna.

Figure 6.7: In-field RSS results for three receiving antenna orientations and nine positions, transmit drone (TX) with fixed vertical up antenna orientation.

However, without the isolation needed to validate these measurements and drone body effects in the elevation plane, no definitive models have been developed or validated in

simulation. Regardless, the dependence on the drone position and antenna orientation was observed throughout these experiments. As previously outlined in Section 1.2, all of our experiments used omnidirectional dipole antennas with a characteristic torus-like radiation pattern in the plane that the antenna is orientated in (Figs. 1.3 & 1.4). Similar to our results in Chapter 5, there is an observed dependence on the elevation angle of the transmit-receive pair that is characteristic of the radiation pattern of an omnidirectional antenna.

As expected, when the receiving antenna is orientated vertically, the drone in the immediate horizontal plane experiences a higher RSS. Similarly, when the receiving antenna is orientated horizontally, the positions above and below the immediate horizontal plane generally experience a higher RSS. While the receiving angle of 0 degrees in Fig. 6.7c matches this predicted behavior, it fails to explain the difference in RSS between the positions directly above and below (± 90 degrees) compared to the positions at the angles of ± 56 degrees. Even with the increased receiver gain in the elevation plane due to the receiving drone's horizontal antenna orientation, if the transmitter produced a perfect omnidirectional pattern it would be expected that the positions directly above and below the transmitting drone would capture the least amount of radiated energy when compared to those at a horizontal separation. However, from this in-field experiment, it is clear that this is not the case. The complex gain based directivity effects experienced by the transmitting drone body, similar to the observed diversity in RSS along the walls in Chapter 5, has yet to be fully characterized and validated for the development of an accurate model. This is a key component that we plan to explore in detail within the multi-dimensional drone-flight-enabled infrastructure.

At this point in our simulation work, we plan to perform several experiments within our indoor infrastructure to move towards a more controlled understanding of the unique three-dimensional aspects that we have identified thus far. The simultaneous multi-dimensional capture capability, as well as the highly precise control of drone position and orientation, will enable us to fully characterize the unique effects from the perspective of a drone-based

receiver and transmitter. Furthermore, due to the dynamic and configurable nature of the SDRs, it is possible to quickly switch the surrounding fixed antennas to receiving or transmitting elements, effectively separating the undesired drone induced variables we faced in the three-dimensional experiment. These insights will enable the validation of multiple drone-based scenarios as well as the dynamic switching or movement of antenna positions and orientations providing an isolated characterization to enhance the simulation environment with a more comprehensive overview of how a practical multi-dimensional multi-drone network will perform.

CHAPTER 7

Related Work

There are several existing works that fall into two broad categories relating to our efforts: (*i.*) using drones as tools within wireless research, such as assessing propagation or improving path planning and control systems algorithms, and (*ii.*) the development of distributed testbeds used to evaluate various forms of wireless communication technologies and coordination.

For example, in [3–5], their understanding of wireless drone performance within cellular networks comes from simulation-based experiments and limited in-field measurements. They demonstrate the unique signal propagation perspective that drones experience on cellular networks when operating in low-altitude environments. In assessing three-dimensional drone communication performance, [10] made use of IEEE 802.11 to measure and characterize drone-to-ground and drone-to-drone links in an outdoor environment using GPS positioning. They provided insight into how the antenna pattern and orientation have impacts on path loss and throughput on a drone platform. In [11], they used a fixed-wing drone to further explore how antenna type and orientation affected achievable throughput. In the work servicing IoT devices with groups of mobile drones [6], they showed via simulation a dramatic reduction in transmit power by optimizing path planning algorithms to service a group of IoT devices with a required bit error rate.

In MIT's Indoor Multi-Vehicle Flight Testbed [7], they coordinate several drones at once and provide accurate localization within an indoor space to assess control systems performance for various missions managing the health of vehicles in the network. There was no mention of the wireless link characteristics that were associated with the various vehicle con-

trol scenarios. The Real-time indoor Autonomous Vehicle test ENvironment (RAVEN) [9] addressed control and path planning algorithms for various vehicle types including quadcopters, fixed-wing planes, and ground-based vehicles. They focused on mission planning and high-level task assignment while balancing vehicle health and factors of uncertainty. In [8], they used a simulation environment to develop multiple drone coordination and control algorithms and validated them in an indoor environment with the aid of visual tracking for localization.

Several testbeds focus on distributed and coordinated wireless technologies. The PAWR Project [12] is helping to develop various emerging technologies such as massive MIMO and 5G connectivity. Lund University built a large array of 100 antennas to better understand and assess the performance of a practical massive MIMO testbed [14]. In FlockLab [13], the authors outlined the creation of a wireless testbed that provided a synchronous method of observing distributed events in wireless embedded systems. The Open Access Research Testbed for Next-Generation Wireless Networks (ORBIT) [15] provided a large scale wireless testbed for indoor reproducibility as well as an outdoor network testbed to test real-world scenarios. In AirShare [17] they proposed a novel method of sharing a reference clock to independent wireless nodes in a distributed manner for use in distributed MIMO and rate adaptation applications. In contrast to these efforts, we build a programmable testbed around a flyable space to inspect drone networks.

CHAPTER 8

Conclusion

In this work, we described our experience and lessons learned from building a drone-flight-enabled wireless isolation chamber, which allows in-depth evaluation of the complex spatial relationships that are experienced in drone communications. To do so, we first built an open-source drone platform that allowed us to directly interface with an indoor localization system and programmatically position drones for a given amount of time. Next, we designed a wireless data acquisition system with a family of SDRs over the outside of the flyable space in the testbed, which presented challenges for synchronization and data logging. Then we demonstrated the culmination of this integration with a highly-controlled experiment from the same transmitter mounted on a drone and show a significant difference in signal strength throughout the facility due to the three-dimensional aspects of the channel/radiation pattern and possibly the drone body. Finally, we demonstrated how our experimental measurements can be leveraged to simulate multi-dimensional drone networks on a practical scale. In the future, the facility will be used to evaluate dynamic antenna switching and MIMO algorithms to and from a single drone and from networks of drones.

BIBLIOGRAPHY

[1] UAS by the numbers. https://www.faa.gov/uas/resources/by_the_numbers/, Feb. 2020. 1

[2] FAA aerospace forecast fiscal years 2019-2039. https://www.faa.gov/data_research/aviation/aerospace_forecasts/media/FY2019-39_FAA_Aerospace_Forecast.pdf, 2019. 1

[3] Vijaya Yajnanarayana, Y.-P. Eric Wang, Shiwei Gao, Siva D. Muruganathan, and Xingqin Lin. Interference mitigation methods for unmanned aerial vehicles served by cellular networks. *CoRR*, abs/1802.00223, 2018. 1, 44

[4] Drones and networks: Ensuring safe and secure operations, Dec. 2019. 1, 44

[5] Xingqin Lin, Richard Wiren, Sebastian Euler, Arvi Sadam, Helka-Liina Maattanen, Siva Muruganathan, Shiwei Gao, Y-P Eric Wang, Juhani Kauppi, Zhenhua Zou, et al. Mobile network-connected drones: Field trials, simulations, and design insights. *IEEE Vehicular Technology Magazine*, 14(3):115–125, 2019. 1, 44

[6] Mohammad Mozaffari, Walid Saad, Mehdi Bennis, and Merouane Debbah. Mobile internet of things: Can UAVs provide an energy-efficient mobile architecture?, Jul. 2016. 1, 44

[7] M. Valenti, B. Bethke, D. Dale, A. Frank, J. McGrew, S. Ahrens, J. P. How, and J. Vian. The MIT indoor multi-vehicle flight testbed. In *Proceedings 2007 IEEE International Conference on Robotics and Automation*, pages 2758–2759, Apr. 2007. 1, 44

[8] N. Michael, D. Mellinger, Q. Lindsey, and V. Kumar. The GRASP multiple micro-UAV testbed. *IEEE Robotics Automation Magazine*, 17(3):56–65, Sep. 2010. 1, 45

[9] J. P. How, B. Behihke, A. Frank, D. Dale, and J. Vian. Real-time indoor autonomous vehicle test environment. *IEEE Control Systems Magazine*, 28(2):51–64, Apr. 2008. 1, 45

[10] Evşen Yanmaz, Robert Kuschnig, and Christian Bettstetter. Achieving air-ground communications in 802.11 networks with three-dimensional aerial mobility. In *2013 Proceedings IEEE INFOCOM*, pages 120–124. IEEE, 2013. 1, 44

[11] C. Cheng, P. Hsiao, H. T. Kung, and D. Vlah. Performance measurement of 802.11a wireless links from UAV to ground nodes with various antenna orientations. In *Proceedings of 15th International Conference on Computer Communications and Networks*, pages 303–308, Oct. 2006. 1, 44

[12] Platforms for Advanced Wireless Research. https://advancedwireless.org/, Mar. 2020. 1, 45

[13] R. Lim, F. Ferrari, M. Zimmerling, C. Walser, P. Sommer, and J. Beutel. Flocklab: A testbed for distributed, synchronized tracing and profiling of wireless embedded systems. In *2013 ACM/IEEE International Conference on Information Processing in Sensor Networks (IPSN)*, pages 153–165, Apr. 2013. 1, 45

[14] J. Vieira, S. Malkowsky, K. Nieman, Z. Miers, N. Kundargi, L. Liu, I. Wong, V. Öwall, O. Edfors, and F. Tufvesson. A flexible 100-antenna testbed for massive MIMO. In *2014 IEEE Globecom Workshops (GC Wkshps)*, pages 287–293, Dec. 2014. 1, 45

[15] D. Raychaudhuri, I. Seskar, M. Ott, S. Ganu, K. Ramachandran, H. Kremo, R. Siracusa, H. Liu, and M. Singh. Overview of the ORBIT radio grid testbed for evaluation of next-generation wireless network protocols. In *IEEE Wireless Communications and Networking Conference, 2005*, volume 3, pages 1664–1669 Vol. 3, Mar. 2005. 1, 45

[16] Mark Berman, Jeffrey S. Chase, Lawrence Landweber, Akihiro Nakao, Max Ott, Dipankar Raychaudhuri, Robert Ricci, and Ivan Seskar. Geni: A federated testbed for innovative network experiments. *Computer Networks*, 61:5 – 23, 2014. Special issue on Future Internet Testbeds – Part I. 1

[17] Omid Abari, Hariharan Rahul, Dina Katabi, and Mondira Pant. Airshare: Distributed coherent transmission made seamless. In *2015 IEEE Conference on Computer Communications (INFOCOM)*, pages 1742–1750. IEEE, 2015. 1, 45

[18] Y. Shi, E. Johnson, J. Wensowitch, and J. Camp. A measurement study of user-induced propagation effects for uhf frequency bands. In *2017 14th Annual IEEE International Conference on Sensing, Communication, and Networking (SECON)*, pages 1–9, 2017. 2

[19] Hui Liu, Jialin He, John Wensowitch, Dinesh Rajan, and Joseph Camp. Architecture and experimental evaluation of context-aware adaptation in vehicular networks. *EURASIP Journal on Wireless Communications and Networking*, 2020(1):1–20, 2020. 2

[20] Y. Shi, R. Enami, J. Wensowitch, and J. Camp. UABeam: UAV-based beamforming system analysis with in-field air-to-ground channels. In *2018 15th Annual IEEE International Conference on Sensing, Communication, and Networking (SECON)*, 2018. 2

[21] Y. Shi, R. Enami, J. Wensowitch, and J. Camp. Measurement-based characterization of LOS and NLOS drone-to-ground channels. In *WCNC*, 2018. 2

[22] M. Badi, J. Wensowitch, D. Rajan, and J. Camp. Experimental evaluation of antenna polarization and elevation effects on drone communications. In *Proceedings of the 22nd International ACM Conference on Modeling, Analysis and Simulation of Wireless and Mobile Systems*, pages 211–220, 2019. 2

[23] Y. Shi, J. Wensowitch, A. Ward, M. Badi, and J. Camp. Building UAV-based testbeds for autonomous mobility and beamforming experimentation. In *2018 IEEE International Conference on Sensing, Communication and Networking (SECON Workshops)*, pages 1–5, 2018. 2

[24] Matrice 100 specs. https://www.dji.com/matrice100/info, Mar. 2020. viii, 5, 14

[25] Aakif Mairaj, Asif I Baba, and Ahmad Y Javaid. Application specific drone simulators: Recent advances and challenges. *Simulation Modelling Practice and Theory*, 2019. 7

[26] Sabur Baidya, Zoheb Shaikh, and Marco Levorato. Flynetsim: An open source synchronized UAV network simulator based on ns-3 and ardupilot. In *Proceedings of the 21st ACM International Conference on Modeling, Analysis and Simulation of Wireless and Mobile Systems*, pages 37–45, 2018. 7

[27] J. Modares, N. Mastronarde, and K. Dantu. Realistic network simulation in the UB-ANC aerial vehicle network emulator. In *2017 IEEE Conference on Computer Communications Workshops (INFOCOM WKSHPS)*, pages 66–71, 2017. 7

[28] S. A. Hadiwardoyo, C. T. Calafate, J. Cano, Y. Ji, E. Hernández-Orallo, and P. Manzoni. 3D simulation modeling of UAV-to-car communications. *IEEE Access*, 7:8808–8823, 2019. 7

[29] A. Y. Javaid, W. Sun, and M. Alam. UAVSim: A simulation testbed for unmanned aerial vehicle network cyber security analysis. In *2013 IEEE Globecom Workshops (GC Wkshps)*, pages 1432–1436, 2013. 7

[30] M. Rice and M. Jensen. Multipath propagation for helicopter-to-ground MIMO links. In *2011 - MILCOM 2011 Military Communications Conference*, pages 447–452, 2011. 12

[31] T. J. Willink, C. C. Squires, G. W. K. Colman, and M. T. Muccio. Measurement and characterization of low-altitude air-to-ground MIMO channels. *IEEE Transactions on Vehicular Technology*, 65(4):2637–2648, 2016. 12

[32] T. Zhou, C. Tao, and L. Liu. LTE-assisted multi-link MIMO channel characterization for high-speed train communication systems. *IEEE Transactions on Vehicular Technology*, 68(3):2044–2051, 2019. 12

[33] Michael G Wing, Aaron Eklund, and Loren D Kellogg. Consumer-grade global positioning system (GPS) accuracy and reliability. *Journal of forestry*, 103(4):169–173, 2005. 14

[34] X. Bao, Z. Xiong, S. Sheng, Y. Dai, S. Bao, and J. Liu. Barometer measurement error modeling and correction for UAH altitude tracking. In *2017 29th Chinese Control And Decision Conference (CCDC)*, pages 3166–3171, 2017. 14

[35] Jussi Parviainen, Jussi Kantola, and J Collin. Differential barometry in personal navigation. In *2008 IEEE/ION Position, Location and Navigation Symposium*, pages 148–152. IEEE, 2008. 14

[36] Jinsil Lee, Eunjeong Hyeon, Minchan Kim, and Jiyun Lee. Vertical position error bounding for integrated GPS / barometer sensors to support unmanned aerial vehicle (UAV). In *ICAS*, 2016. 14

[37] Hskt technology specifications. https://www.indotraq.com/, Mar. 2020. 19

[38] White rabbit switch. https://sevensols.com/index.php/products/white-rabbit-switch/. 22